Available online at www.sciencedirect.com
ScienceDirect
Physics of the Earth and Planetary Interiors 160 (2007) 124–142
PHYSICS OF THE EARTH AND PLANETARY INTERIORS
www.elsevier.com/locate/pepi

Intrusion of ultramafic magmatic bodies into the continental crust: Numerical simulation

Taras V. Gerya*, Jean-Pierre Burg

Department of Geosciences, ETH-Zurich, CH-8092 Zurich, Switzerland

Received 26 June 2006; received in revised form 12 October 2006; accepted 30 October 2006

Abstract

Intrusions of ultramafic bodies into the lower density continental crust are documented for a large variety of tectonic settings spanning continental shields, rift systems, collision orogens and magmatic arcs. The intriguing point is that these intrusive bodies have a density higher by 300–500 kg m^{-3} than host rocks. Resolving this paradox requires an understanding of the emplacement mechanism. We have employed finite differences and marker-in-cell techniques to carry out a 2D modeling study of intrusion of partly crystallized ultramafic magma from sublithospheric depth to the crust through a pre-existing magmatic channel. By systematically varying the model parameters we document variations in intrusion dynamics and geometry that range from funnel- and finger-shaped bodies (pipes, dikes) to deep seated balloon-shaped intrusions and flattened shallow magmatic sills. Emplacement of ultramafic bodies in the crust lasts from a few kyr to several hundreds kyr depending mainly on the viscosity of the intruding, partly crystallized magma. The positive buoyancy of the sublithospheric magma compared to the overriding, colder mantle lithosphere drives intrusion while the crustal rheology controls the final location and the shape of the ultramafic body. Relatively cold elasto-plastic crust ($T_{\mathrm{Moho}} = 400\,^{\circ}\mathrm{C}$) promotes a strong upward propagation of magma due to the significant decrease of plastic strength of the crust with decreasing confining pressure. Emplacement in this case is controlled by crustal faulting and subsequent block displacements. Warmer crust ($T_{\mathrm{Moho}} = 600\,^{\circ}\mathrm{C}$) triggers lateral spreading of magma above the Moho, with emplacement being accommodated by coeval viscous deformation of the lower crust and fault tectonics in the upper crust. Strong effects of magma emplacement on surface topography are also documented. Emplacement of high-density, ultramafic magma into low-density rocks is a stable mechanism for a wide range of model parameters that match geological settings in which partially molten mafic–ultramafic rocks are generated below the lithosphere. We expect this process to be particularly active beneath subduction-related magmatic arcs where huge volumes of partially molten rocks produced from hydrous cold plume activity accumulate below the overriding lithosphere.

Keywords: Ultramafic intrusions; Magma emplacement; Mantle melts; Numerical modeling; Magmatic arcs

1. Introduction

Magmatism is one of the major material and geochemical transfer processes in the earth (e.g., Ramberg, 1981; Petford et al., 2000). Volcanism refers to spectacular magma eruptions that fascinate the general public but the less flamboyant effects of underground magma expansion, called plutonism, remain captivating to earth scientists. Since James Hutton conceived the idea of plutonism in the late 18th century (e.g., Ellenberger, 1994) the formation of large magma bodies, the plutons, eludes full understanding. Research on the topic has, however, been much focused on the emplacement

* Corresponding author. Tel.: +41 44 633 6623; fax: +41 44 633 1065.
E-mail address: taras.gerya@erdw.ethz.ch (T.V. Gerya).

0031-9201/$ – see front matter © 2006 Elsevier B.V. All rights reserved.
doi:10.1016/j.pepi.2006.10.004

of granitic magma (e.g., Pitcher, 1979), which is particularly abundant on continents (e.g., Rudnick and Gao, 2004).

Field studies and geophysical imaging indicate that granitic and non-granitic plutons have both very variable and comparable shapes and sizes (e.g., Best and Christiansen, 2001; Petford, 1996; Cruden and McCaffrey, 2001; Bolle et al., 2002). The dimensions of plutons are therefore rock-type independent. It is generally accepted that plutons grow by collecting and transferring melt from a deep source to higher emplacement levels. Melting (anatexis and dehydration melting of hydrous minerals) of rocks generates these melts, with felsic to intermediate compositions when the source is the continental crust, or mafic and ultramafic compositions when partial melting affects the upper mantle (e.g., Rudnick and Gao, 2004). However, evidence for sublithospheric magma sources indicates that transfer of non-kimberlitic magma also occurs on a larger scale, through the lithosphere (e.g., Anderson, 1994; Schmidt and Poli, 1998; Ernst et al., 2005; Wright and Klein, 2006). Many conceptual, pencil models sketched this notion and its variations (e.g., Pons et al., 1992; Glazner et al., 2004). They all involve a gravity-controlled instability (e.g., Cruden, 1990; Paterson and Fowler, 1993) but none conclusively explains how space is made for the growing pluton. This question has generated two schools of thoughts: forceful emplacement, implying that space is made by the body forces of the magma pushing aside wall rocks, or passive emplacement of melt flowing into fissures formed by regional stresses. This duality may represent two mechanical end members sensitive to the relative rates of magma production and deformation (e.g., Hutton, 1988), the relative proportions of regional, thermal and buoyancy stresses (e.g., Spera, 1980; Furlong and Meyers, 1985; Vigneresse, 1995), the depth of emplacement, and several other mechanisms leading to vertical, horizontal and temporal gradients (Paterson and Fowler, 1993; Vigneresse and Clemens, 2000).

This necessarily short and non-extensive summary shows that a complex system of physical parameters, including magma driving pressure, local and regional stresses, and the physical properties of the intruding material, determine the emplacement conditions and final shape of plutons. While accepting the conventional ideas concerning plutonism, we are confronting three intriguing questions: (1) how can magma move from sublithospheric molten regions to shallower storage chambers? (2) How high-density, ultramafic and mafic magma can ascend into the lower density crust, at odds with the common acceptance that mafic and ultramafic magma stays deep and forms the lower crust (e.g., Rudnick, 1995; Rudnick and Gao, 2004) and (3) how temperature-sensitive rheologies of both magma and country rocks together influence the emplacement of such ultramafic–mafic magmas?

We decided to take advantage of recent progress in hardware and software capabilities to generate two-dimensional visco-elasto-plastic numerical models of ulramafic intrusion emplacement incorporating in particular the temperature-sensitive properties of both magma and country rocks. Our principal goal is to understand stable mechanisms of emplacement and unravel the principal physical parameters controlling variations in intrusion geometry and emplacement dynamics.

2. Model specification

2.1. General setting

Thermomechanical modeling of magma intrusion is numerically challenging because it involves simultaneous and intense deformation of materials with very contrasting rheological properties: the country, crustal rocks are visco-elasto-plastic while the intruding magma is a low viscosity, complex fluid (e.g., Pinkerton and Stevenson, 1992). We employ the 2D code I2ELVIS (Gerya and Yuen, 2003a), which is based on finite differences with a marker-in-cell technique. The code allows for the accurate conservative solution of the governing equations on a rectangular fully staggered Eulerian grid. New developments allow for both large viscosity contrasts and strong deformation of visco-elasto-plastic multiphase flow. The code was tested for a variety of problems by comparing results with both analytical solutions (Gerya and Yuen, 2003a) and analogue sandbox experiments (Buiter et al., 2006). The color boundaries (Fig. 1) are passive features used to visualize external and internal structural patterns.

2.2. Initial model box

The 1100 km × 300 km model (Fig. 1) was specially designed for the study of dynamic processes during emplacement of partially molten mantle rocks from a sublithospheric magmatic source region (SMSR) to the crust. A non-uniform rectangular grid with maximum cell size 10 km × 10 km allows small cells of 0.25 km × 0.50 km in the upper central, 40 km wide and 40 km deep "intrusion area" atop the prescribed magmatic channel explained below (Fig. 1). The initial thermal structure of the lithosphere is as usually assumed with a 35 km thick crust corresponding to a sectioned

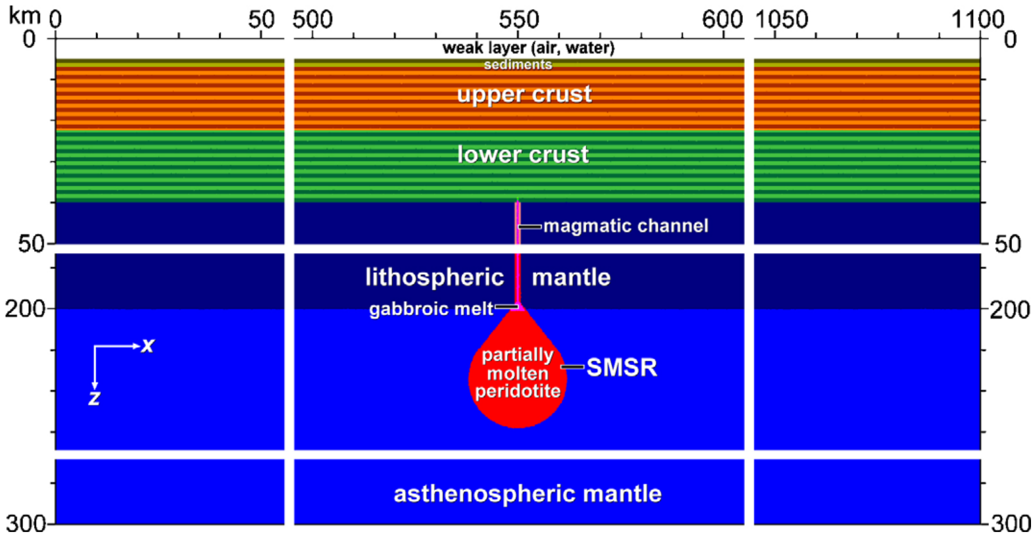

Fig. 1. 2D numerical setting of this study. The lithospheric and asthenospheric mantles have the same physical properties, different colors are used for better visualization of deformation and structural development. This is also true for the passive color-layering in the upper and the lower crust. Initial and boundary conditions are detailed in the text.

linear temperature profile limited by 0 °C at the surface, 400 °C at the bottom of the crust and 1300 °C at 195 km depth. The temperature gradient in the asthenospheric mantle is 0.6 °C/km below 195 km depth. There is no horizontal heat flow across the vertical boundaries. An infinity-like "constant external temperature" along the bottom (Burg and Gerya, 2005) implies 2140 °C at 1300 km depth. This condition, which is satisfied far below the model, allows us to vary both temperatures and vertical heat fluxes along the lower box boundary. Thanks to this numerical device, a set of experiments could be made to investigate the influence of initial thermal structures that affect modeled crustal and mantle rheology on the intrusion processes.

The velocity boundary conditions are free slip at the upper boundary and no slip at the left and right boundaries, which are neither diverging nor converging, i.e., there is no background deformation field. Material flow is allowed in both downward and upward directions through the lower boundary (Fig. 1). An infinity-like "external free slip" condition along the bottom (Burg and Gerya, 2005) implies free slip at the 1300 km depth, i.e., far below the lower box boundary.

The SMSR and the magmatic channel across the lithospheric mantle were prescribed. The SMSR and the 0.2 km thick median channel composed of gabbroic melt were prescribed a uniform magmatic temperature, which was varied between 1300 and 1500 °C for different numerical experiments. This is the presumed temperature range at the head of hydrous thermal–chemical mantle plumes (e.g., Gerya and Yuen, 2003b; Gerya et al., 2004a; Table 3). We emphasise that the modeled SMSR is nothing more than a thermally and chemically distinct region of hydrated, partially molten mantle rocks and not a chamber of fully molten magma. Partially molten material has a much lower viscosity than the surrounding dry mantle (e.g., Pinkerton and Stevenson, 1992) and can move through the magmatic channel as crystal mush. In that sense the SMSR is equivalent to a magma reservoir. According to our linear melting model (Table 2) this hydrated region has 10–30 vol.% of melt varying with depth and temperature. Though the bulk composition of the SMSR in our model is ultramafic, the melt composition within the SMSR depends on the degree of melting and thus varies between mafic and ultramafic.

The magmatic channel is a vertical, 1.5 km wide zone characterized by a wet olivine rheology (Ranalli, 1995) and a low 1 MPa plastic strength. Test experiments revealed that higher plastic strength precludes the ascent of magma from the SMSR while lower strength does not significantly alter simulation results. The mantle lithosphere surrounding the channel has a dry olivine rheology (Ranalli, 1995) and a high plastic strength corresponding to a dry Byerlee's law (Brace and Kohlstedt, 1980). By implementing a pre-existing hot and weak magmatic channel we accepted the general assumption that magma rises from the source area through any lithospheric perturbation. Natural hot channels may originate at an early magmatic stage due to the rapid and localized upward percolation of hot mobile fluids/melts, which are differentiation products at the top of the SMSR. Mechanisms of localized upward fluid/melt transport include hydrofracture (e.g., Clemens and Mawer, 1992), diffusion (e.g., Scambelluri and Philippot, 2001), porous flow (e.g., Scott and Stevenson, 1986; Connolly and Podladchikov, 1998; Vasilyev et al., 1998; Ricard et al., 2001) and reactive flow (e.g., Spiegelman and Kelemen, 2003). The point is that fluid percolation diminishes the plastic strength of rocks through an increase in pore fluid pressure, which in turn allows massive ascent of partially molten rocks through the lithosphere. Propagation of magmatic rocks from the channel into the crust develops spontaneously and is mainly controlled by crustal rheology and density.

We employed a simplified layered structure of the 35 km thick continental crust with three common lithological units (top to bottom): sediments (2 km), upper crust (15.5 km) and lower crust (17.5 km). We tested the effects of a variation in the composition of both the upper and lower crust by simultaneously varying the standard density and ductile flaw laws (Table 2): the "felsic composition" is prescribed low density (2800 kg m^{-3}) and weak ductile rheology corresponding to a wet quartz flow law (Ranalli, 1995) while the "mafic composition" has a higher density (3000 kg m^{-3}) and a stronger ductile rheology dominated by plagioclase creep (Ranalli, 1995).

2.3. Topography

Emplacement of large magmatic bodies high in the crust causes space problems that roof uplift and isostatic flexure may largely compensate. Because such vertical movement would affect the topographic evolution of adjacent regions, we have implemented a very low viscosity (10^{13} to 10^{16} Pa s), initially 5 km thick layer above the crust (Fig. 1). This creates large (10^3 to 10^6) viscosity contrasts between the numerical crust and the weak layer, closely matching a free surface condition atop the Earth's crust. Test experiments have shown that choosing lower viscosities of the weak layer do not affect the topography development. The density of this weak layer is either 1 kg m^{-3} (air, above the z = 5 km level, with z = 0 = top of the box) or 1000 kg m^{-3} (water, below the z = 5 km "water level", which is also the initial crustal surface level). The interface between this very weak layer and the top of the continental crust is treated as a free erosion/sedimentation surface, which evolves dynamically according to the transport equation solved in Eulerian coordinates at each time-step (Gerya and Yuen, 2003b):

$$\frac{\partial z_{es}}{\partial t} = v_z - v_x \frac{\partial z_{es}}{\partial t} - v_s + v_e, \tag{1}$$

where z_{es} is the vertical position of the surface as a function of the horizontal distance x; v_z and v_x are the vertical and horizontal components of the material velocity vector at the surface, respectively; v_s and v_e are sedimentation and erosion rates, respectively, and correspond to the relation:

$$v_s = 0, \quad v_e = 0.3\,\text{mm/yr}, \quad \text{when} \quad z < 5\,\text{km},$$

$$v_s = 0.3\,\text{mm/yr}, \quad v_e = 0, \quad \text{when} \quad z \geq 5\,\text{km},$$

2.4. Melt crystallization and partial melting

Crystallization of intruding magma and, to some extent, partial melting of host rocks are two important and coeval processes during plutonism (e.g., Marsh, 1982; Best and Christiansen, 2001) because they affect the density and the rheology of both intruding and intruded rocks, respectively. The presented numerical models allow gradual crystallization of magma and partial melting of the crust in the pressure–temperature domain between the wet solidus and dry liquidus of corresponding rocks (Table 2). As a first approximation, the volumetric fraction of melt M at constant pressure is assumed to increase linearly with temperature according to the relations (Gerya and Yuen, 2003b; Burg and Gerya, 2005):

$$M = 0, \quad \text{at} \quad T \leq T_{\text{solidus}}, \tag{2a}$$

$$M = \frac{T - T_{\text{solidus}}}{T_{\text{liquidus}} - T_{\text{solidus}}}, \quad \text{at} \quad T_{\text{solidus}} < T < T_{\text{liquidus}}, \tag{2b}$$

$$M = 1, \quad \text{at} \quad T \geq T_{\text{liquidus}}, \tag{2c}$$

where T_{solidus} and T_{liquidus} are the wet solidus and dry liquidus temperatures of the considered rock, respectively (Table 2).

The effective density, ρ_{eff}, of partially molten rocks is calculated from:

$$\rho_{\text{eff}} = \rho_{\text{solid}} - M(\rho_{\text{solid}} - \rho_{\text{molten}}) \tag{3}$$

where ρ_{solid} and ρ_{molten} are the densities of solid and molten rock, respectively, which vary with pressure and temperature according to the relation:

$$\rho_{P,T} = \rho_0[1 - \alpha(T - T_0)][1 + \beta(P - P_0)] \tag{4}$$

where ρ_0 is the standard density at P_0 = 0.1 MPa and T_0 = 298 K; α and β are the thermal expansion and compressibility coefficients, respectively (see Table 1 for notations).

Table 1
Abbreviations and units

Symbol	Meaning
A_D (MPa^{-n} s^{-1})	Material constant
Cp (J kg^{-1} K^{-1})	Isobaric heat capacity
E (kJ mol^{-1})	Activation energy
G (Pa)	Plastic potential
H_r, H_a, H_s (W m^{-3})	Radioactive, adiabatic and shear heat production
k (W m^{-1} K^{-1})	Thermal conductivity
M	Volume fraction of melt
n	Stress exponent
P, P_{solid} (Pa)	Dynamic pressure (mean stress on solids)
P_{fluid} (Pa)	Pore fluid pressure
Q_L (kJ/kg^{-1})	Latent heat of melting
t (s)	Time
T (K)	Temperature
$T_{liquidus}$, $T_{solidus}$ (K)	Liquidus and solidus temperature of a rock
V (J MPa^{-1} mol^{-1})	Activation volume
v_x, v_z (m s^{-1})	Horizontal and vertical components of velocity vector
x, z (m)	Horizontal and vertical coordinates
Z	Viscoelasticity factor
α (K^{-1})	Thermal expansion coefficient
β (Pa^{-1})	Compressibility coefficient
χ (s^{-1})	Plastic multiplier
$\dot{\varepsilon}_{ij}$ (s^{-1})	Components of the strain rate tensor
η (Pa s)	Viscosity
λ	Pore fluid pressure coefficient: $\lambda = P_{fluid}/P_{solid}$
μ (Pa)	Shear modulus
ρ (kg m^{-3})	Density
σ_{II} (Pa^2)	Second invariant of the deviatoric stress tensor
σ_{ij} (Pa)	Components of the deviatoric stress tensor

The effect of latent heating due to equilibrium melting/crystallization is included implicitly by increasing the effective heat capacity (Cp_{eff}) and thermal expansion (α_{eff}) of the partially crystallized/molten rocks ($0 < M < 1$), calculated as (Burg and Gerya, 2005):

$$Cp_{eff} = Cp + Q_L\left(\frac{\partial M}{\partial T}\right)_P, \tag{5a}$$

$$\alpha_{eff} = \alpha + \rho\frac{Q_L}{T}\left(\frac{\partial M}{\partial P}\right)_T, \tag{5b}$$

where Cp is the heat capacity of the solid rock, and Q_L is the latent heat of melting of the rock (Table 2).

2.5. Rheological model

We employed a visco-elasto-plastic rheology with the bulk strain rate $\dot{\varepsilon}_{ij}$ including three respective compo-

Table 2
Material properties[a] used in 2D numerical experiments

Material	ρ_0 (kg m^{-3})	k (W m^{-1} K^{-1})	$T_{solidus}$ (K)	$T_{liquidus}$ (K)	Q_L (kJ/kg)	H_r (μW m^{-3})	Flow law	E (kJ mol^{-1})	n	A_D (MPa^{-n} s^{-1})	V (J/(MPa mol))	μ (GPa)
Sediments	2600	$[0.64+807/(T+77)] \times \exp(0.00004P_{MPa})$	–	–	–	1.75	Wet quartzite	154	2.3	$10^{-3.5}$	0	10
Felsic crust	2800 (Solid)	$[0.64+807/(T+77)] \times \exp(0.00004P_{MPa})$	$889+17900/(P+54)+20200/(P+54)^2$ at $P<1200$ MPa	$1262+0.09P$	300	1	Wet quartzite	154	2.3	$10^{-3.5}$	0	25
	2500 (Molten)		$831+0.06P$ at $P>1200$ MPa									
Mafic crust, gabbro of the magma chamber	3000 (Solid)	$[1.18+474/(T_K+77)] \times \exp(0.00004P_{MPa})$	$973-70400/(P+354)+77800000/(P+354)^2$ at $P<1600$ MPa	$1423+0.105P$	380	0.25	Plagioclase An_{75}	238	3.2	$10^{-3.5}$	0	25
	2800 (Molten)		$935+0.0035P+0.0000062P^2$ at $P>1600$ MPa									
Lithosphere–asthenosphere mantle	3300	$[0.73+1293/(T_K+77)] \times \exp(0.00004P_{MPa})$	–	–	–	0.022	Dry olivine	532	3.5	$10^{4.4}$	8	67
Peridotite of the magma chamber	3250 (Solid)	$[0.73+1293/(T_K+77)] \times \exp(0.00004P_{MPa})$	$1240+49800/(P+323)$ at $P<2400$ MPa	$2073+0.114P$	300	0.022	Wet olivine	470	4	$10^{3.3}$	8	67
	2900 (Molten)		$1266–0.0118P+0.0000035P^2$ at $P>2400$ MPa									
References[b]	1, 2	3	4	4, 6	1,2	1	5	5	5	5	1,5	1

[a] $Cp = 1000$ J/kg, $\alpha = 3 \times 10^{-5}$ K^{-1}, $\beta = 1 \times 10^{-5}$ Mpa^{-1} for all rock types.
[b] (1) Turcotte and Schubert (2002), (2) Bittner and Schmeling (1995), (3) Clauser et al. (1995), (4) Schmidt and Poli (1998), (5) Ranalli, 1995, (6) Hess, 1989.

Table 3
Parameters[a] of conducted numerical experiments

Model	Upper crust	Lower crust	SMSR				Crustal strength			T_{Moho} (°C)	Shape[b]	Depth below the surface (km)						
			Diameter (km)	C (MPa)	η_{min} (Pa s)	T_0 (°C)	λ_0	C (MPa)	γ_{cr}			0 kyr	5 kyr	10 kyr	50 kyr	100 kyr	150 kyr	200 kyr
1 (kocd)	Mafic	Mafic	24	1	10^{16}	1400	0.65	3	0.1	400	Vn-I	34.6	34.6	34.6	31.7	26.5	24.5	23.5
2 (kocg)	Mafic	Mafic	24	1	10^{16}	1400	0.65	1	0.1	400	V	34.6	34.6	34.5	28.2	6.3	1.7	0.9
3 (koch)	Mafic	Mafic	24	1	10^{16}	1400	0.65	2	0.1	400	V	34.6	34.6	34.5	30.7	12.4	2.0	0.6
4 (koci)	Mafic	Mafic	24	1	10^{16}	1400	0.65	3	0.05	400	Vn-I	34.6	34.6	34.6	26.3	10.6	8.4	7.9
5 (kocj)	Mafic	Mafic	24	1	10^{16}	1400	0.65	3	0.2	400	S-I	34.6	34.6	34.6	33.6	30.8	28.9	28.1
6 (kock)	Mafic	Mafic	24	1	10^{16}	1400	0.65	1	0.05	400	Va	34.6	34.6	34.5	15.6	2.8	0.5	0.2
7 (kocl)	Mafic	Mafic	24	1	10^{16}	1350	0.65	1	0.05	400	Vn	34.6	34.6	34.6	16.7	4.2	1.9	1.4
8 (kocm)	Felsic	Felsic	24	1	10^{16}	1400	0.65	1	0.1	400	Is	34.6	34.6	34.5	34.1	33.7	32.9	32.3
9 (kocn)	Felsic	Mafic	24	1	10^{16}	1400	0.65	1	0.1	400	Sb-V	34.6	34.6	34.5	27.3	10.7	7.0	5.9
10 (koco)	Mafic	Mafic	24	1	10^{16}	1400	0.67	1	0.1	400	Va-T	34.6	34.6	34.6	29.1	4.4	0.8	0.6
11 (kocp)	Mafic	Mafic	24	1	10^{13}	1400	0.67	1	0.1	400	T	34.6	26.8	0	0	0	0	0
12 (kocq)	Mafic	Mafic	24	1	10^{14}	1400	0.67	1	0.1	400	T	34.6	26.6	0	0	0	0	0
13 (kocr)	Mafic	Mafic	24	1	10^{15}	1400	0.67	1	0.1	400	T	34.6	34.3	32.9	0	0	0	0
14 (kocs)	Mafic	Mafic	24	1	10^{17}	1400	0.67	1	0.1	400	In	34.6	34.6	34.5	34.5	34.5	34.5	34.4
15 (kocu)	Felsic	Felsic	24	1	10^{13}	1400	0.65	1	0.1	400	Vab	34.6	31.7	4.2	2.8	2.7	2.7	2.6
16 (kocv)	Mafic	Mafic	24	1	10^{16}	1350	0.67	1	0.1	400	I	34.6	34.4	34.4	29.7	9.5	5.4	4.3
17 (kocw)	Mafic	Mafic	24	1	10^{16}	1450	0.67	1	0.1	400	Vb	34.6	34.6	34.6	22.2	4.6	1.1	0.6
18 (kocx)	Mafic	Mafic	24[a]	1	10^{16}	1400	0.67	1	0.1	400	–	34.6	34.5	34.5	34.4	34.4	34.4	34.4
19 (kocy)	Mafic	Mafic	24	1	10^{16}	1400	0.83	1	0.1	400	Vb	34.6	34.4	34.4	19.9	9.4	5.3	2.3
20 (kocz)	Mafic	Mafic	24	1	10^{16}	1400	0.50	1	0.1	400	Van	34.6	34.5	34.5	27.1	4.4	0.7	0.4
21 (koda)[c]	Mafic	Mafic	24	1	10^{16}	1400	0.66	1	0.1	400	Vn	34.6	34.5	34.4	17.4	5.8	4.5	4.4
22 (kodb)[c]	Mafic	Mafic	24	1	10^{16}	1400	0.67	1	0.1	400	Vn	34.6	34.5	34.4	18.9	6.1	4.4	4.4
23 (kodc)	Mafic	Mafic	24	1	10^{16}	1300	0.67	1	0.1	400	S	34.6	34.5	34.5	33.8	20.4	12.8	11.6
24 (kodd)	Mafic	Mafic	24	1	10^{16}	1500	0.67	1	0.1	400	Vb	34.6	34.4	34.4	17.0	2.9	0.6	0.4
25 (kode)	Mafic	Mafic	24	1	10^{16}	1400	0	1	0.1	400	I-T	34.6	34.4	34.4	34.0	33.6	33.4	31.4
26 (kodf)	Mafic	Mafic	24	1	10^{13}	1400	0	1	0.1	400	Va-T	34.6	31.5	0.5	0	0	0	0
27 (kodg)	Mafic	Mafic	24[d]	1	10^{16}	1400	0.67	1	0.1	400	–	34.9	34.9	34.9	34.9	34.9	34.9	34.9
28 (kodh)	Mafic	Mafic	20	1	10^{16}	1400	0.67	1	0.1	400	I	34.6	34.4	34.4	31.0	13.2	6.0	5.4
29 (kodi)	Mafic	Mafic	30	1	10^{16}	1400	0.67	1	0.1	400	Vab-T	34.6	34.4	34.4	18.3	0.8	0.1	0
30 (kodj)	Mafic	Mafic	24	1	10^{16}	1400	0.67	1	0.1	600	I-V	34.6	34.3	34.3	32.9	30.8	27.8	5.6
31 (kodk)	Felsic	Felsic	24	1	10^{16}	1400	0.67	1	0.1	600	O	34.6	34.2	33.9	30.3	28.0	25.4	23.2
32 (kodl)	Mafic	Mafic	24	1	10^{13}	1400	0.67	1	0.1	600	Vab-T	34.6	33.2	3.2	0	0	0	0
33 (kodm)	Felsic	Felsic	24	1	10^{13}	1400	0.67	1	0.1	600	Oa	34.6	31.3	26.8	10.5	10.4	10.4	10.4
34 (kodn)	Mafic	Mafic	24[e]	1	10^{16}	1400	0.67	1	0.1	400	Va-T	34.6	34.4	34.3	22.2	0.8	0	0
35 (kodo)	Mafic	Mafic	24[e]	1	10^{13}	1400	0.67	1	0.1	400	T	34.6	3.0	0	0	0	0	0
36 (kodp)	Mafic	Mafic	24[f]	1	10^{16}	1400	0.67	1	0.1	400	In	34.6	34.5	34.5	34.4	34.3	31.8	8.2

Table 3 (*Continued*)

Model	Upper crust	Lower crust	SMSR				Crustal strength			T_{Moho} (°C)	Shape[b]	Depth below the surface (km)						
			Diameter (km)	C (MPa)	$\eta_{\min}$ (Pa s)	T_0 (°C)	λ_0	C (MPa)	γ_{cr}			0 kyr	5 kyr	10 kyr	50 kyr	100 kyr	150 kyr	200 kyr
37 (kodq)	Mafic	Mafic	24[f]	1	10^{13}	1400	0.67	1	0.1	400	Vbs	34.6	34.3	33.9	24.3	12.2	12.1	12.1
38 (kodr)	Mafic	Mafic	24[g]	1	10^{16}	1400	0.67	1	0.1	400	V	34.6	34.4	34.4	29.0	7.9	2.5	1.0
39 (kods)	Mafic	Mafic	24	1	10^{16}	1400	0.67	1	0.1	400[h]	Va-T	34.6	34.5	34.5	27.5	4.5	0.7	0.4
40 (kodt)[i]	Mafic	Mafic	24	1	10^{16}	1400	0.67	1	0.1	400[h]	V	34.6	34.5	34.5	27.6	7.0	3.5	2.2

[a] Small amount of gabbroic melt: no gabbroic melt in the SMSR, gabbroic melt in the magmatic channel is restricted by shallow 30–95 km depths.
[b] Culminate shape of the body after emplacement (Figs. 7 and 8): O—balloon-shaped; V—funnel-shaped; S—sickle-shaped; I—finger-shaped; T—nappe(sill)-shaped; a—asymmetric; b—broad; n—narrow; s—short.
[c] Maximal viscosity of all rocks is set to 10^{26} Pa s (10^{23} Pa s is the default value for other experiments).
[d] No gabbroic melt.
[e] Shallower SMSR: bottom of the lithosphere and initial position of the SMSR (Fig. 1) are displaced upward by 50 km.
[f] Deeper SMSR: bottom of the lithosphere and initial position of the SMSR (Fig. 1) are displaced downward by 50 km.
[g] Medium amount of gabbroic melt: gabbroic melt in the magmatic channel only, no gabbroic melt in the SMSR.
[h] Concave initial geotherm with 50 °C higher temperature in the middle crust.
[i] Free slip lower boundary condition.

nents:

$$\dot{\varepsilon}_{ij} = \dot{\varepsilon}_{ij(\mathrm{viscous})} + \dot{\varepsilon}_{ij(\mathrm{elastic})} + \dot{\varepsilon}_{ij(\mathrm{plastic})} \tag{6}$$

where

$$\dot{\varepsilon}_{ij(\mathrm{viscous})} = \frac{1}{2\eta}\sigma_{ij},$$

$$\dot{\varepsilon}_{ij(\mathrm{elastic})} = \frac{1}{2\mu}\frac{\mathrm{D}\sigma_{ij}}{\mathrm{D}t},$$

$$\dot{\varepsilon}_{ij(\mathrm{plastic})} = 0, \quad \text{when} \quad (\sigma_{\mathrm{II}})^{1/2} < \sigma_{\mathrm{yield}} \quad \text{and}$$

$$\dot{\varepsilon}_{ij(\mathrm{plastic})} = \chi\frac{\partial G}{\partial \sigma_{ij}} = \chi\frac{\sigma_{ij}}{2\sigma_{\mathrm{II}}{}^{1/2}}, \quad \text{when} \quad (\sigma_{\mathrm{II}})^{1/2} < \sigma_{\mathrm{yield}}.$$

where $\mathrm{D}\sigma_{ij}/\mathrm{D}t$ is objective co-rotational time derivative of deviatoric stress component σ_{ij}, σ_{yield} the plastic yield strength for given rock, $G = (\sigma_{\mathrm{II}})^{1/2}$ the plastic potential of non-dilatant material and χ is plastic multiplier satisfying the plastic yielding condition $(\sigma_{\mathrm{II}})^{1/2} = \sigma_{\mathrm{yield}}$, where $\sigma_{\mathrm{II}} = 1/2\sigma_{ij}\sigma_{ij}$ is second deviatoric stress invariant.

The viscosity of solid rocks ($M \leq 0.1$) essentially depends on stress, pressure and temperature. It is defined in terms of the second deviatoric stress invariant (Ranalli, 1995) as:

$$\eta = \left(\frac{4}{\sigma_{\mathrm{II}}}\right)^{(n-1)/2} \frac{F^n}{A_{\mathrm{D}}} \exp\left(\frac{E+V}{RT}\right), \tag{7}$$

where A_{D}, E, V and n are experimentally determined flow law parameters (Table 2). F is a dimensionless coefficient depending on the type of experiments on which the flow law is based (Ranalli, 1995). For example:

$$F = \frac{2^{(1-n)/n}}{3^{(1+n)/2n}}, \quad \text{for triaxial compression and}$$
$$F = 2^{(1-2n)/n}, \quad \text{for simple shear.}$$

10^{13} to 10^{16} and 10^{23} to 10^{26} Pa s are the lower and upper values for viscosity of all types of crustal rocks in the presented simulations (Table 3).

According to geological observations, fault tectonics, hence plastic deformation of the crust, play a significant role during plutonic emplacement resulting from fluid/melt percolation along forming fracture zones (e.g., Clemens and Mawer, 1992). The plastic yield strength of rocks under fluid-present conditions strongly depends on the ratio between solid (P_{solid}) and fluid (P_{fluid}) pressure according to (Ranalli, 1995; Brace and Kohlstedt, 1980):

$$\sigma_{\mathrm{yield}} = C + (N_1 P + N_2)(1 - \lambda) \tag{8}$$

where $\lambda = P_{\text{fluid}}/P_{\text{solid}}$ is the pore fluid pressure factor and C is the residual strength (cohesion) of rocks "fully" pressurized by internal fluid ($P_{\text{fluid}} = P_{\text{solid}}$, $\lambda = 1$), $P_{\text{solid}} = P$ corresponds to mean stress on solids (i.e., dynamic non-lithostatic solid pressure), N_1 and N_2 are empirical constants defined experimentally (Brace and Kohlstedt, 1980) for dry fractured crystalline rocks ($N_1 = 0.85$, $N_2 = 0$ when $P < 200$ MPa and $N_1 = 0.6$, $N_2 = 60$ MPa when $P > 200$ MPa). During intrusion, most intensive percolation of magmatic fluids is expected to follow the pattern of fractured rocks formed along spontaneously propagating fault zones. Fluid supply will then increase the pore fluid pressure along the fault zones, thus strongly lowering the plastic yield strength of the fractured rocks. This will in turn further localize deformation along the continuously weakening fault zones. Under such circumstances the plastic strength of fractured rocks will be in inverse correlation with the amount of continuous plastic deformation experienced by the rocks. In order to model this process in a simplified way, the fluid pressure factor λ for a given model rock increases with plastic strain:

$$\gamma_{\text{plastic}} = \int_t \left(\tfrac{1}{2}\dot{\varepsilon}_{ij(\text{plastic})}\dot{\varepsilon}_{ij(\text{plastic})}\right)^{1/2}$$

$\mathrm{d}t$ experienced by the rock,

$$\lambda = 1 - (1-\lambda_0)\left(1 - \frac{\gamma_{\text{plastic}}}{\gamma_{\text{cr}}}\right),$$

when $\gamma_{\text{plastic}} < \gamma_{\text{cr}}$, and $\lambda = 1$,

when $\gamma_{\text{plastic}} \geq \gamma_{\text{cr}}$, (9)

where λ_0 is the initial (before plastic yielding) pore fluid pressure factor for the rock and γ_{cr} is the critical plastic strain required for weakening the rock by percolating fluid (i.e., the strain necessary for reaching condition $P_{\text{fluid}} = P_{\text{solid}}$, $\lambda = 1$). We explored the influence of varying λ_0 and γ_{cr} of crustal rocks on the dynamics of intrusion (Table 3) by varying the parameters of the plastic flow laws through the entire crust, knowing that the brittle strength of dry rocks is insensitive to their composition (Byerlee's law, Brace and Kohlstedt, 1980).

The effective viscosity η of molten rocks ($M > 0.1$) was calculated by using the formula (Bittner and Schmeling, 1995; Pinkerton and Stevenson, 1992):

$$\eta = \eta_0 \exp\left[2.5 + (1-M)\left(\frac{1-M}{M}\right)^{0.48}\right] \tag{10}$$

where η_0 is an empirical parameter depending on rock composition, $\eta_0 = 10^{13}$ Pa s is taken for molten mafic–ultramafic rocks (i.e., $1\times10^{14} \leq \eta \leq 2\times10^{15}$ Pa s for $0.1 \leq M \leq 1$) and $\eta_0 = 5\times10^{14}$ Pa s (i.e., $6\times10^{15} \leq \eta \leq 8\times10^{16}$ Pa s for $0.1 \leq M \leq 1$) for felsic rocks (Bittner and Schmeling, 1995).

2.6. Conservation equations and numerical implementation

We have considered 2D creeping flow wherein both thermal and chemical buoyant forces are included, along with heating from adiabatic compression and viscous dissipation in the heat conservation equation.

We have adopted a Lagrangian frame (Gerya and Yuen, 2003a) in which the heat conservation equation with thermal conductivity $k(T,P,C)$ (Table 2) depending on rock composition (C), pressure and temperature takes the form:

$$\rho Cp\left(\frac{\mathrm{D}T}{\mathrm{D}t}\right) = -\frac{\partial q_x}{\partial x} - \frac{\partial q_z}{\partial z} + H_\mathrm{r} + H_\mathrm{a} + H_\mathrm{S} \tag{11}$$

$$q_x = -k(T,P,C)\frac{\partial T}{\partial x},$$

$$q_z = -k(T,P,C)\frac{\partial T}{\partial z},$$

$$H_\mathrm{a} = T\alpha\left(v_x\frac{\partial P}{\partial x} + v_z\frac{\partial P}{\partial z}\right),$$

$$H_\mathrm{S} = \sigma_{xx}(\dot{\varepsilon}_{xx} - \dot{\varepsilon}_{xx(\text{elastic})}) + \sigma_{zz}(\dot{\varepsilon}_{zz} - \dot{\varepsilon}_{zz(\text{elastic})}) + 2\sigma_{xz}(\dot{\varepsilon}_{xz} - \dot{\varepsilon}_{xz(\text{elastic})}),$$

where $\mathrm{D}T/\mathrm{D}t$ represents the substantive time derivative, H_r is the radioactive heating that depends on rock composition (Table 2), and other notations are given in Table 1.

The conservation of mass is approximated by the incompressible continuity equation (e.g., Turcotte and Schubert, 2002):

$$\frac{\partial v_x}{\partial x} + \frac{\partial v_z}{\partial z} = 0 \tag{12}$$

The 2D Stokes equations for creeping flow take the form:

$$\frac{\partial \sigma_{xx}}{\partial x} + \frac{\partial \sigma_{xz}}{\partial z} = \frac{\partial P}{\partial x} \tag{13}$$

$$\frac{\partial \sigma_{zz}}{\partial z} + \frac{\partial \sigma_{xz}}{\partial x} = \frac{\partial P}{\partial z} - g\rho(T,P,C,M) \tag{14}$$

The density $\rho(T,P,C,M)$ depends explicitly on temperature, pressure, rock composition and melt fraction. Deviatoric stress components σ_{ij} in Eqs. (13) and (14) are formulated from visco-elasto-plastic constitutive relationships (Eq. (6)) by using first-order finite differences in time $(\mathrm{D}\sigma_{ij}/\mathrm{D}t) = (\sigma_{ij} - \sigma_{ij}^{o})/\Delta t$ in order to represent time derivatives of elastic stresses (e.g., Moresi et al., 2003):

$$\sigma_{ij} = 2\eta_{\mathrm{vp}}\dot{\varepsilon}_{ij}Z + \sigma^{o}_{ij}(1 - Z) \tag{15}$$

$$Z = \frac{\Delta t\mu}{\Delta t\mu + \eta_{\mathrm{vp}}},$$

$$\eta_{\mathrm{vp}} = \eta, \quad \text{when} \quad (\sigma_{\mathrm{II}})^{1/2} < \sigma_{\mathrm{yield}}, \quad \text{and}$$

$$\eta_{\mathrm{vp}} = \eta\frac{(\sigma_{\mathrm{II}})^{1/2}}{\eta\chi + (\sigma_{\mathrm{II}})^{1/2}}, \quad \text{when} \quad (\sigma_{\mathrm{II}})^{1/2} = \sigma_{\mathrm{yield}},$$

in which Δt is elastic time step, σ^{o}_{ij} is the deviatoric stress tensor from the previous time slice corrected for advection and rotation by using a non-diffusive marker-in-cell technique (e.g., Moresi et al., 2003; Gerya and Yuen, 2003a). Z is the viscoelasticity factor and η_{vp} is a viscosity-like parameter computed iteratively to satisfy the plastic yielding condition ($\eta_{\mathrm{vp}} = \eta$ when no plastic yielding occurs). It is worth noting that dynamic (and not depth-dependent lithostatic) pressure was consistently used in all calculations including rheological and melting models, thus taking into account the effects of non-lithostatic pressures in deforming regions of the crust (Petrini and Podladchikov, 2000; Burg and Gerya, 2005; Buiter et al., 2006).

3. Results

Forty configurations (Table 3) were carried out with a finite-difference grid of 325 × 125 irregularly spaced Eulerian points, and with about 2 million markers, in order to capture fine details of the temperature, material, stress and strain rate fields. By varying the experimental parameters we were primarily interested in quantifying the dynamics and the shape of intruding bodies as a function of: (1) the composition and rheology of the magma and host rock and (2) the initial thermal and lithological structure. Reference results are those of Model 2 (Table 3; Figs. 2–4), which used standard parameter values. Similar evolutions were recognized in other models, with variances that are discussed below.

3.1. First-order emplacement history

The numerical intrusion processes typically span a few hundreds kyr (Fig. 2; Table 3) and consist of three main stages: (1) magmatic channel spreading, (2) emplacement and (3) post-intrusive subsidence. The duration of each of these stages strongly depends on model parameters, especially on the viscosity of ascending magma:

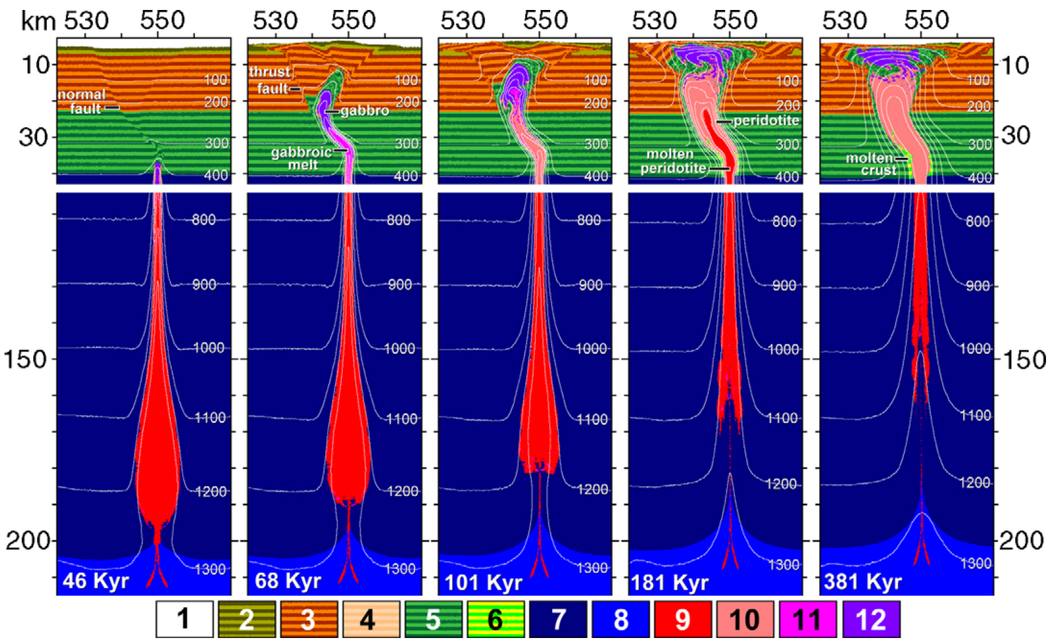

Fig. 2. Enlarged 50 km × 215 km areas of the original 1100 km × 300 km reference Model 2 (Table 3). Distribution of rock layers in the intrusion area during emplacement of the ultramafic body into the crust from below the lithosphere via the magmatic channel. Color code: 1 = weak layer (air, water); 2 = sediments; 3 and 4 = upper crust (3, solid; 4, molten); 5 and 6 = lower crust (5, solid; 6, molten); 7 and 8 = mantle (7, lithospheric; 8, asthenospheric); 9 and 10 = peridotite (9, molten; 10, crystallized); 11 and 12 = gabbro (11, molten; 12, crystallized). Time (kyr) is given in the figures. White numbered lines are isotherms in °C. Vertical scale: depth below the upper boundary of the model.

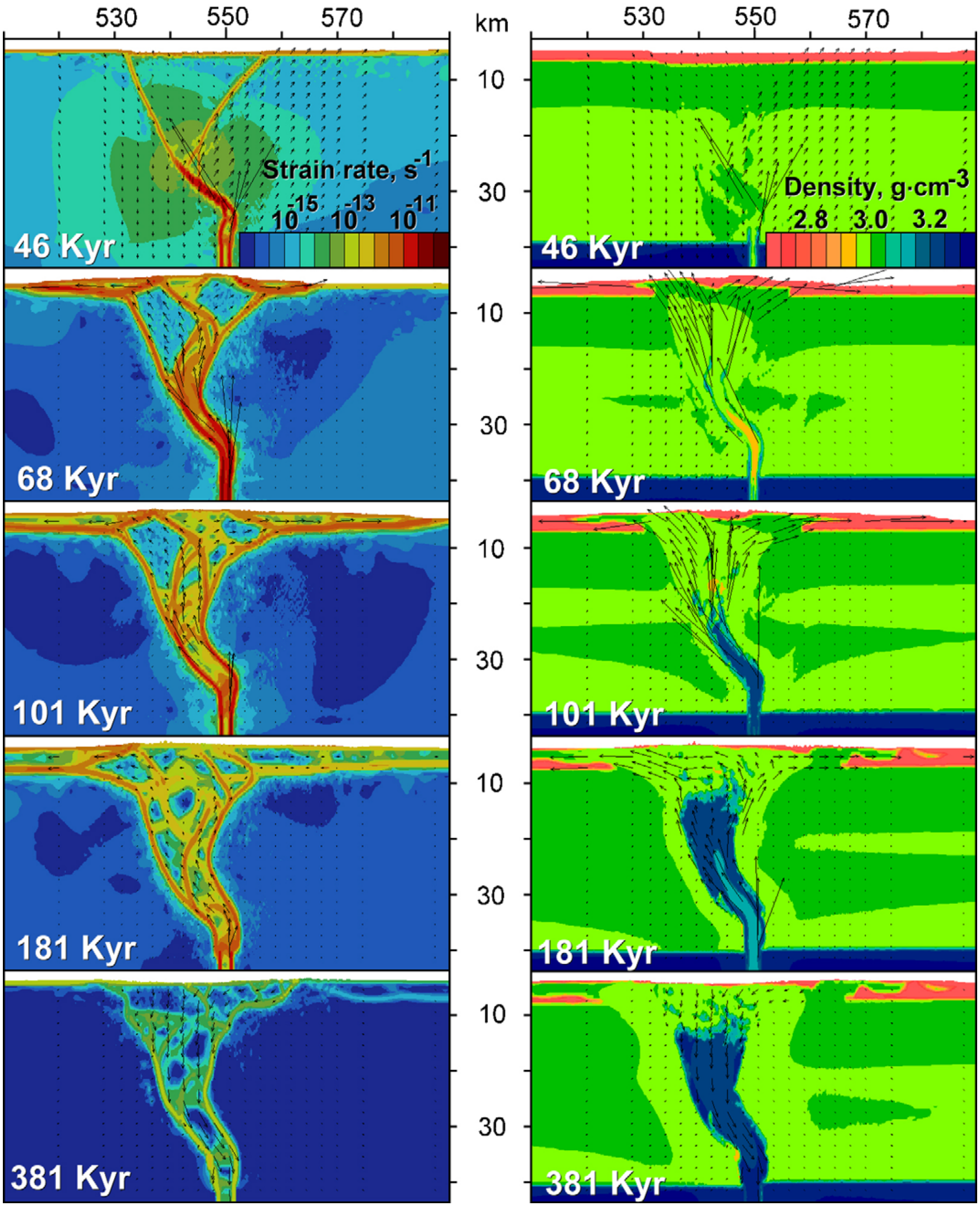

Fig. 3. Enlarged 80 km × 45 km areas of the original 1100 km × 300 km reference Model 2 (Fig. 2; Table 3). Left: Strain rate (square root of second invariant of strain rate tensor $\dot{\varepsilon}_{\mathrm{II}} = 1/2\dot{\varepsilon}_{ij}\dot{\varepsilon}_{ij}$ shown as color code). Right: Density fields for corresponding time kyr stages (note the inverted density contrast between the host crust and the intruding body). Arrows show the calculated velocity field (length of arrows on the first and last sketches is exaggerated by a factor of 3 and 30, respectively).

(1) During channel spreading (Fig. 2, 46 kyr), magma rapidly raises from the SMSR, causing broadening of the weak 1.5 km wide magmatic channel. The lithospheric mantle part of this channel contains an elongated, tear-shaped magmatic body reaching up to 12 km in its widest part. Deformation of the surrounding dry mantle lithosphere accommodates channel widening in a visco-elastic manner in the deeper and warmer part, and elastic in the shallower and colder part. Widening of the channel with depth (Fig. 2, 46 kyr) is related to the viscosity of the lithospheric mantle decreasing with increasing temperature along the geotherm. Channel spreading prompts extension at the base of the

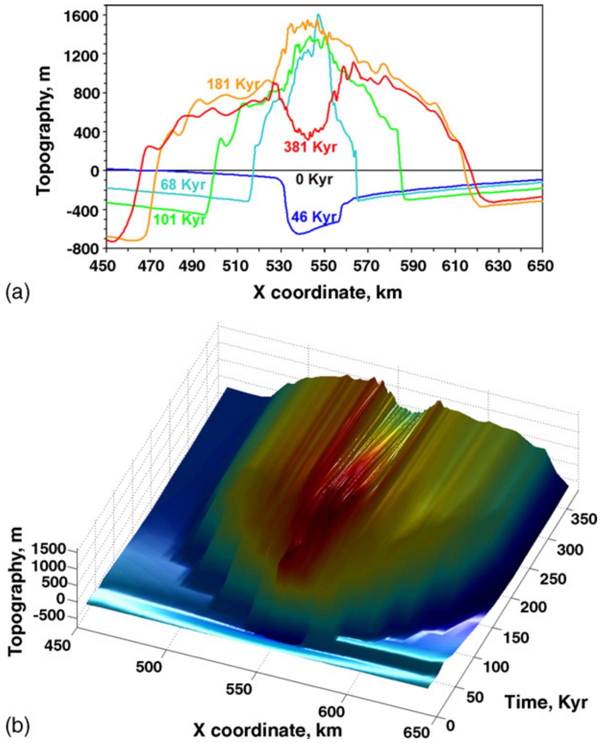

Fig. 4. Evolution of the topography above the intrusion area for the reference Model 2 (Table 3, Figs. 2 and 3). Vertical axis corresponds to the elevation above $z = 5$ km level.

crust, which triggers upwards propagating, conjugate normal faulting (Figs. 2 and 3, 46 kyr, see also Models 1 and 5, Fig. 5c) and surface subsidence in a graben-like depression (see topography profile for 46 kyr in Fig. 4a). Normal fault zones are characterized by low strength and high pore-fluid pressure caused by infiltration of magmatic fluids. Localized pore pressure is the cause for these strongly weakened fault zones to persist during the subsequent emplacement history; however, the normal faults rapidly become inverted into thrusts while the secondary magma chamber inflates and rises in the crust (Figs. 2 and 3, 68 kyr). The strain rate along these faults depends on their width and hence is model-resolution-dependent. In the presented experiments, the width of 0.25–0.5 km results in high strain rates of about 10^{-11} s^{-1} (Fig. 3).

(2) The emplacement stage describes magma penetrating up the crust (Fig. 2, 68–101 kyr) where it expands in secondary magma chambers (Fig. 2, 101–181 kyr). These secondary chambers pervade spaces between tectonic crustal blocks dissected by localized zones of intense plastic deformation (i.e., fault zones, Fig. 3, left column). The density of the intruding magma is still notably higher (by 200–300 kg m^{-3}) than that of the crustal host rocks (Fig. 3, right column, 101–181 kyr) though

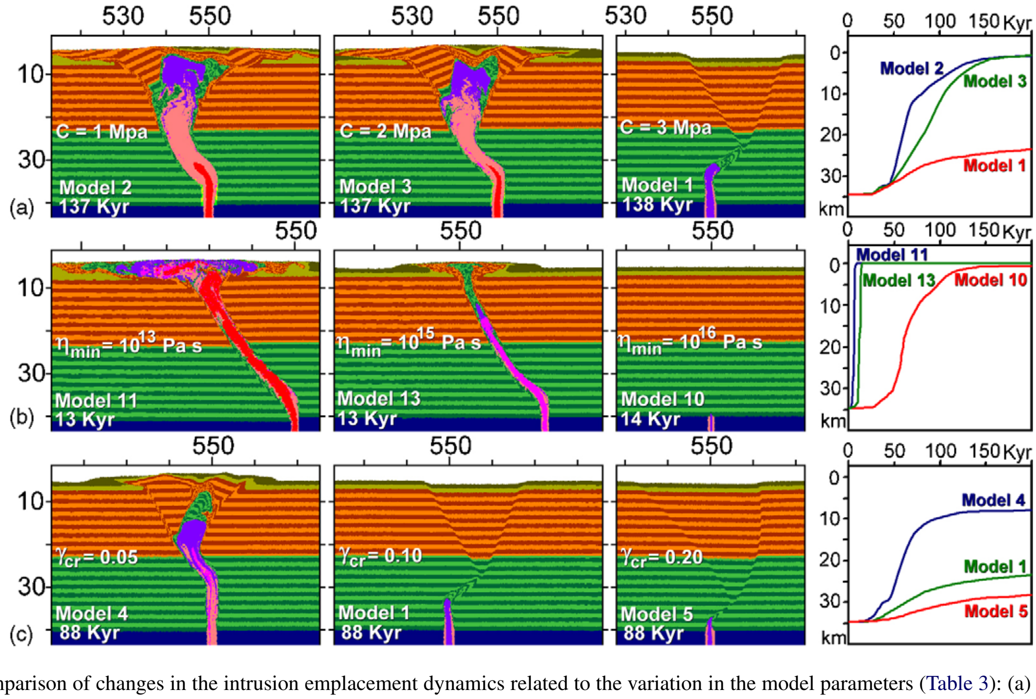

Fig. 5. Comparison of changes in the intrusion emplacement dynamics related to the variation in the model parameters (Table 3): (a) variations in the residual strength of the crust (C); (b) variations in the lower "cutoff" value for the effective viscosity of rocks and melts (η_{min}); (c) variations in the amount of plastic strain necessary for weakening of crustal rocks (γ_{cr}). Rock types are the same as in Figs. 1 and 2.

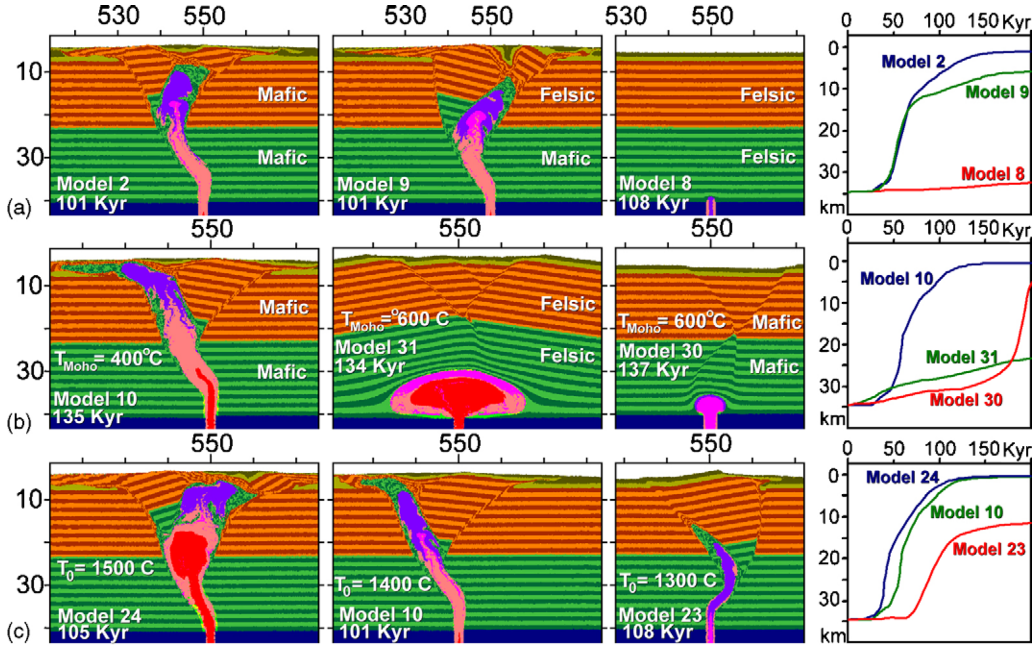

Fig. 6. Comparison of changes in the intrusion emplacement dynamics related to the variation in the model parameters (Table 3): (a) variations in the composition of the crust; (b) variations in the Moho temperature (T_{Moho}); (c) variations in the initial temperature of the SMSR (T_0). Rock types are the same as in Figs. 1 and 2.

it is lower than the density of the non-molten lithospheric mantle. Extrusion of hot, partially molten rocks through the magmatic channel is primarily driven by the density contrast between these partially molten rocks and the mantle lithosphere. To minimize gravitational energy, intrusive rocks of intermediate density should tend to pool along the crust/mantle boundary (Model 31, Fig. 6b). However, as will be discussed later in this paper, this tendency is only realized if the ductile lower crust is relatively weak. In the reference Model 2 (Fig. 2) the lower crust is strong elasto-plastic (therefore, its strength rapidly decreases with decreasing depth, more precisely with decreasing dynamic pressure); in that case, intrusion propagates upward to the upper crust where emplacement requires less mechanical work. The restraining gravitational energy produced by the arrival of a dense intrusion in the less dense crust is compensated and overcome by the positive buoyancy of partially molten rocks in the magmatic channel. This phenomenon is comparable to the penetration of a diapir head into lower density rocks while diapirism is driven by a deep gravitational instability (e.g., Ramberg, 1981; Gerya et al., 2000). It is worth emphasizing that the gravitational balance controls the height of the column of molten rock but not the volume of magmatic rock below and above the Moho. This is expressed in the mechanical equilibrium relation:

$$h_{\mathrm{Channel}}(\rho_{\mathrm{Mantle}} - \rho_{\mathrm{Magma}}) = h_{\mathrm{intrusion}}(\rho_{\mathrm{Magma}} - \rho_{\mathrm{Crust}})$$

where h_{Channel} is the height of the column of magmatic rock in the channel below the Moho, $h_{\mathrm{Intrusion}}$ is the height of magmatic rock above the Moho, ρ_{Mantle}, ρ_{Magma} and ρ_{Crust} are densities of the mantle lithosphere, the intruding magma and the crust, respectively. Since the width of the channel below the Moho is limited by the rigidity of the cold mantle lithosphere, the volume of magma intruding the crust can be much larger than the volume of rock remaining in the channel.

Thrust tectonics affects the topography that shows a 50–150 km wide high broadening above the intrusion (Fig. 4, 68–181 kyr). Associated faulting and block displacements result in specific funnel-shaped magmatic bodies (Fig. 2, 181–381 kyr). The space required to place the intrusive body is mostly resolved by surface uplift and subordinate elastic strain of the crust.

(3) After establishment of the intrusion into the crust, magma continues cooling and crystallizing, which increases the density contrast with the host crust and tends to drive the magmatic body into minor subsidence (Figs. 3 and 4, 181–381 kyr). This subsidence

is effectively responsible for flattening the funnel-shaped body and squeezing parts of intrusive rocks back into the magmatic channel below the Moho (arrows in Fig. 4, 381 kyr). The return down flow is suppressed by increasing the strength of cooling and crystallizing magmatic rocks. 20–40 km wide graben-like depressions of the surface atop the intrusion reflect surface subsidence (Fig. 4, 381 kyr).

3.2. Variations in intrusion dynamics

We systematically studied variations in intrusion dynamics caused by varying model parameters (Table 3, Figs. 5 and 6). Seven variables may separately (and together) accelerate the emplacement stage: (1) decreasing viscosity of the intruding magma (Fig. 5b), (2) decreasing initial (λ_0, compare Models 10 and 25, 11 and 26; Table 2) and residual (C, Fig. 5a) plastic strength of the crust, (3) decreasing the amount of plastic strain necessary for crust weakening (γ_{cr}, Fig. 5c), (4) increasing the effective viscosity of the lower crust by either changing its composition/flow law (Fig. 6a) or decreasing the Moho temperature (Fig. 6b), (5) increasing the initial temperature of the SMSR (Fig. 6c), (6) decreasing the thickness of the mantle lithosphere and the depth of the SMSR below the crust (compare Models 34 and 36, 35 and 37; Table 3) and (7) increasing the amount of lower-density mafic melt in the magmatic channel (Fig. 1; Models 10, 18, 27 and 38; Table 1). The strongest effects are obtained by varying the magma viscosity (Fig. 5b): models with the smallest magma viscosity (10^{13} to 10^{15} Pa s) are characterized by much swifter channel spreading (2–10 kyr) and much faster ascent of magma into the crust (2–5 kyr) than models with moderate (10^{16} Pa s, 30–50 and 50–70 kyr, respectively) and high (10^{17} Pa s, >200 and >300 kyr, respectively, Model 14 in Table 3) viscosity. Faster ascent also speeds up both channel spreading and extension in the lower crust, which prompts plastic failure of the crust and, therefore, shortens the initial channel spreading stage. On the other hand, if the ductile lower crust has low effective viscosity (e.g., felsic composition and/or high "Moho" temperature), extension is accommodated by viscous rather than elasto-plastic deformation, which retards plastic failure and upward propagation of the magmatic channel. This process favors chamber ballooning (Fig. 6a and b).

3.3. Variations in final pluton shapes

Table 3 and Figs. 7 and 8 summarize variations in the culminate shape of the numerical plutons. We qualitatively subdivided these two-dimensional geometries into

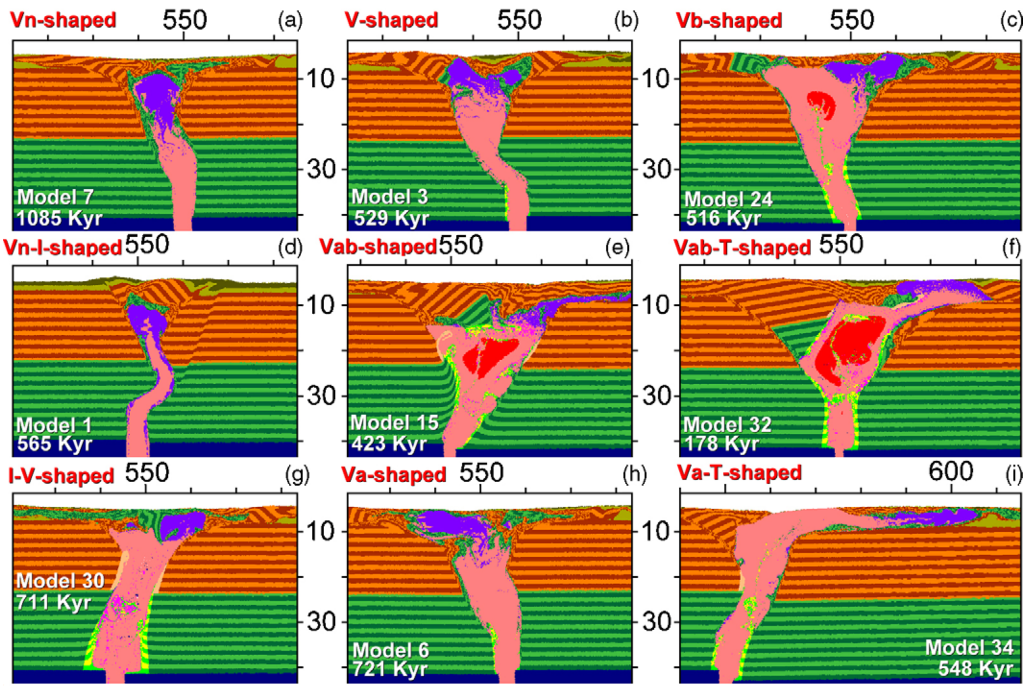

Fig. 7. Major types of culminate shapes of intrusions obtained in numerical experiments due to the variations in the model parameters (Table 3). Red letters denote intrusion shapes: V—funnel-shaped; I—finger-shaped; T—nappe(sill)-shaped; a—asymmetric; b—broad; n—narrow. Rock types are the same as in Figs. 1 and 2.

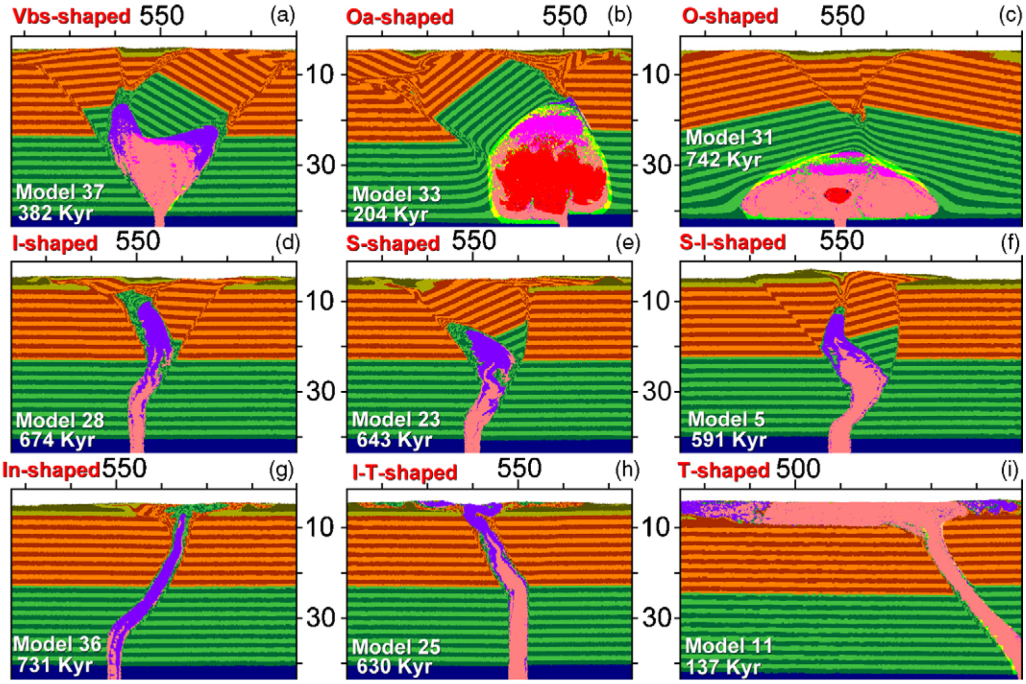

Fig. 8. Major types of culminate shapes of intrusions obtained in numerical experiments due to the variations in the model parameters (Table 3). Red letters denote intrusion shapes: O—balloon-shaped; V—funnel-shaped; S—sickle-shaped; I—finger-shaped; T—napppe(sills)-shaped; a—asymmetric; b—broad; n—narrow; s—short. Rock types are the same as in Figs. 1 and 2.

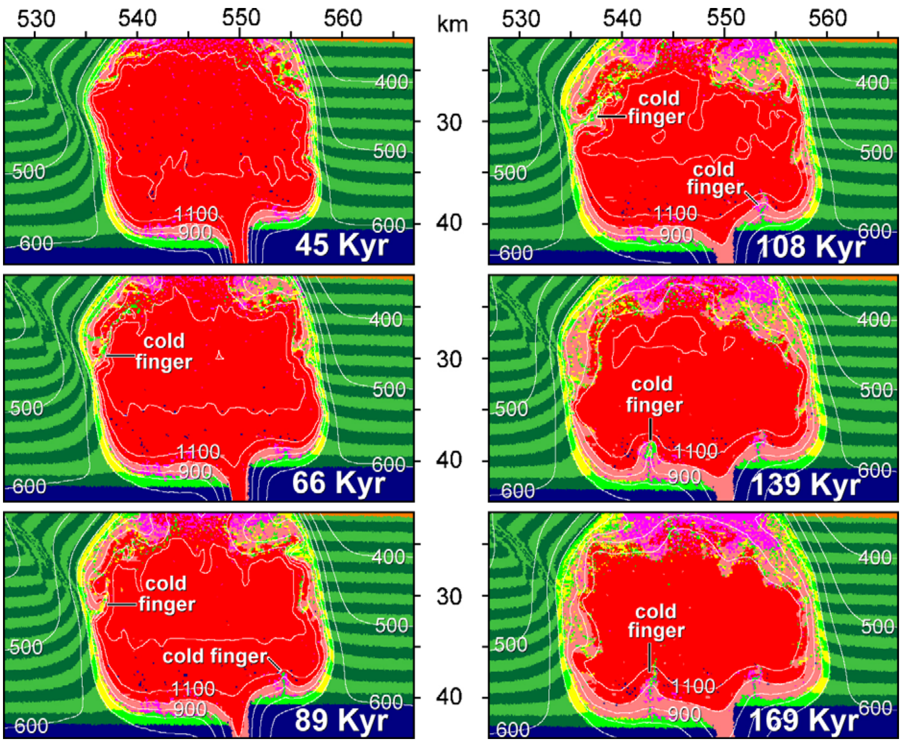

Fig. 9. Development of cold finger phenomena inside the secondary magma chamber due to the partial melting of the host lower crustal rocks. Enlarged 40 km × 22 km areas of the original 1100 km × 300 km Model 33 (Table 3) are shown. Time (kyr) is given in the figures. White numbered lines are isotherms in °C. Rock types are the same as in Figs. 1 and 2.

five major types: funnel-shaped (V, Figs. 2 and 7a–c), finger-shaped (I, Fig. 8d and g), sickle-shaped (S, Fig. 8e), nappe(sill)-shaped (T, Fig. 8i) and balloon-shaped (O, Fig. 8b and c). The first four types are characteristic for an elasto-plastic crust whereas balloon-shaped intrusions typify ductile lower crusts with low viscosity. Table 3 shows that most frequently obtained types are funnel-shaped, as in the reference Model 2 (Fig. 2). Nappe(sill)-like bodies (Fig. 5b) are characteristic for low viscosity magma ascending rapidly through spontaneously forming narrow crustal channel limited by faults and subsequently spreading in the shallow level sill. Intermediate shapes evidently exist between the different types (Table 3, Figs. 7 and 8) such as finger-funnel-shape (Fig. 7d), funnel-nappe shape (Fig. 7f and i), etc. The intrusion geometry may strongly change during emplacement from small finger- and sickle-shaped bodies to large funnel- or nappe-shaped plutons (Figs. 2 and 5b). Small balloon-shaped intrusions can develop into large finger-shaped bodies (Model 30, Figs. 6b and 7g), a metamorphosis related to changes in dominating crustal deformation mechanism (viscous in the warmer and deeper crust and elasto-plastic in the shallower and colder crust) during upward intrusion growth.

The internal structure of intrusions is often complicated by various types of magmatic and crustal inclusions (e.g., Best and Christiansen, 2001). High-resolution models indicate that slices of the lower crust (all the way down to the Moho) are regularly enclaved during the rapid ascent of partially molten rock (e.g., Figs. 2(101–381 kyr), 5a and 7b). Narrow (0.1–2 km wide) lens-like pieces limited by weak faults are often dragged upward along the intrusion boundaries, which is an efficient mechanism for exhuming lower crustal rocks (e.g., Figs. 2(101–381 kyr), 5a and 6b). Another type of inclusion is related to partial melting and buoyant ascent of crustal rocks in form of 0.5–1 km wide "cold fingers" (Gerya et al., 2003, 2004b) into the intrusion (Figs. 7c, e and i, 8b and c and 9). At the time of emplacement, these fingers are characterized by a positive buoyancy along with a negative temperature anomaly (the core is colder than the rim, Fig. 9). The positive buoyancy of these cold fingers could be related to a lower crust more felsic than the intrusive rocks, while lower temperature expresses the inverted vertical temperature gradient (temperature decreases with increasing depth) at the bottom and on the walls of the magma intrusion (Fig. 9).

4. Discussion and geological relevance

The numerical models presented in this study answer the questions brought up to introduce this paper: mafic and ultramafic magma (crystal mush) may ascend from sublithospheric regions to crustal storage chambers through hot channels. Models further show that this is a stable mechanism for a wide range of parameters in accordance with the geological commonness of mafic and ultramafic plutons into various continental crusts (e.g., reviews in Wyllie, 1967; Irvine, 1967; Best and Christiansen, 2001). Ascent is rapid, which is consistent with rare attempts to measure rates of melt movements (Turner et al., 2001). We emphasize that intrusion of mafic and ultramafic magma does not require any background deformation opening a fissure-like deformation zone: a mere rheological perturbation that acts as magma channel is sufficient to allow, under far-field static conditions, the passage of large amounts of mafic–ultramafic magma. This point is applicable to ultramafic plutons that have intruded stable cratons like the Paleoproterozoic Kola Peninsula (e.g., Kogarko, 1987) and the Aldan Shield in Siberia (e.g., Elianov and Andreev, 1991); it is also relevant to large ring dyke complexes on planets devoid of plate tectonics (e.g., Montesi, 2001). Supporting this, surface uplift followed by subsidence due to mafic–ultramafic magmatism is a characteristic feature of large basaltic provinces (e.g., Maclennan and Lovell, 2002). Obviously, any background tectonics creating zones of localized deformation, i.e., magmatic channel in the crust, will render all these processes even easier.

A large sublithospheric magmatic source region (SMSR) was prescribed in the presented models. Geologically, this implementation means that a significant amount of partially molten mafic–ultramafic rock should be first produced below the lithosphere. Although magma reservoirs elude geophysical survey (Glazner et al., 2004) the existence of large source regions is a geologically legitimate assumption for at least three tectonic settings: (1) where hot asthenospheric material is drawn to shallow depths by the spreading at mid-ocean ridges (e.g., Sparks and Parmentier, 1991; Braun et al., 2000; Rabinowicz and Ceuleneer, 2005) and above thermal sublithospheric plumes that are thought to produce hot spots on the Earth (e.g., Sleep, 2006) and other planets (Coffin and Eldholm, 1994; Head and Coffin, 1997). (2) In regions of continental extension (rift systems of Europe, e.g., Xu et al., 1998, and East Africa, e.g., Lin et al., 2005; Ernst et al., 2005); in these examples, geochemical information indicates that even small melt volumes may penetrate the lithosphere (Bedini et al., 1997). Mafic intrusions in the lower crust of recent (e.g., Mjelde et al., 2002) and older (e.g., Muentener et al., 2000) passive margins may be equivalent to experimental secondary magma chambers, but in extensional settings. (3) Below subduction-related magmatic arcs (e.g., Irvine, 1967; Taylor, 1967); arc formation requires large and long-lived, primarily mantle-derived magma reservoirs (e.g., Turner et al., 2000; Dungan et al., 2001); multiphase metasomatism of mantle wedge peridotites found as xenoliths in arc lavas demonstrate that magma source regions (in our sense) are sublithospheric (Arai et al., 2007) while mantle diapirism may lead to back-arc spreading (e.g., Iwamori, 1991). It is common knowledge that several geochemical characteristics of arc magmas originate through partial melting of depleted mantle peridotite fluxed by slab-derived (hence from beneath the intruded lithosphere) fluids/melts enriched in more mobile incompatible elements (e.g., McCulloch and Gamble, 1991; Brenan et al., 1995; Borg et al., 1997; Harry and Green, 1999). Also, recent numerical modeling studies of subduction associated with mantle wedge hydration predict that huge amounts of partially molten rock forming SMSR can be generated at asthenospheric depths below subduction-related magmatic arcs due to hydrous cold plume activity (Gerya and Yuen, 2003b; Gerya et al., 2004a, 2006; Gorczyk et al., 2006).

We qualitatively subdivided the modeled magmatic bodies into five major types that refer to classical plutonic shapes described in the geological literature (e.g., Best and Christiansen, 2001 and many text books). Funnel shapes would refer to lopoliths and cone sheets, finger shapes to plugs, pipes, necks, dikes, sickle shapes to crescentic plutons (Schwerdtner et al., 1983), nappe shapes to sills, sheets and laccoliths, and finally balloon shapes to stocks, bosses, blisters and many "diapirs". We have pointed out that funnel, finger, sickle and nappe shapes refer to the elasto-plastic behavior of the crust whereas balloon-shaped intrusions occur if the ductile lower crust has low viscosity. How high-density magma will traverse the crust essentially depends on rheology of the lithospheric mantle and its density contrast with the rising magma. In models, the buoyancy forces alone are not responsible for upward magma expulsion. Viscous and plastic strain of both the lithosphere and the crust takes an active role and makes an important contribution in injecting high-density magma into lower density rocks. These new conclusions indicate that the shape and depth of mafic–ultramafic intrusions bear important significance in terms of lithospheric rheology and magma viscosity (Fig. 10).

Another noticeable result concerns internal plutonic structures. High-resolution models clearly indicate that layering is dynamically produced during magma emplacement with older, colder magma capping (Fig. 2) and sheathing (Figs. 5 and 6) incoming magma. This bulk situation includes smaller-scale syn-intrusion folding of layering and magma interfaces. The various

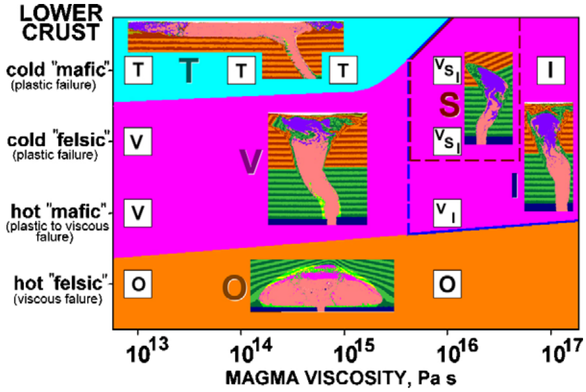

Fig. 10. Stability of major intrusion shapes as a function of lower crust rheology and magma viscosity. Open rectangles show conditions of performed numerical experiments (Table 3). Black letters in these rectangles correspond to obtained intrusion shapes: O—balloon-shaped; V—funnel-shaped; S—sickle-shaped; I—finger-shaped; T—nappe(sills)-shaped. Rock types are the same as in Figs. 1 and 2.

model arrangements displayed in Figs. 2 and 5–9 are reminiscent of incremental plutonic assemblages with concentric and lateral compositional zoning along with syn-magmatic structures reported in the literature (e.g., Sparks et al., 1985; Bédard et al., 1988; Stel, 1991). Flattening of the magma body in the latest stage is consistent with compaction during magma solidification (Parsons and Becker, 1987) and sideways "ballooning" effects often described as late emplacement phenomenon recorded around plutons (e.g., Brun and Pons, 1981; Bateman, 1985; Pons et al., 1992).

Models also readily show that the dichotomy between "forceful" and "stoping" mechanisms is semantic, since both are combined and reflect variations of host rock rheology, hence likely local stress regimes around the intrusion, as was argued by Hogan and Gilbert (1997) for granitic sheets.

It is obvious that 2D models like those made here simulate planar structures that are equivalent to dikes rather then pipes. Introducing the third dimension may notably affect the dynamics and geometry of emplacement. For example, topographic elevation (Fig. 4) is significantly exaggerated in 2D models containing the emplacement of laterally infinite intrusions. Significant effects could also be related to the variation in geometry of trans-lithospheric channels in 3D. Laterally extensive planar channels modeled here are likely to produce dikes and lens-like bodies in case of elasto-plastic crust and laterally elongated balloons in case of weak ductile crust. On the other hand, fingered channels will produce pipes and necks in the strong elasto-plastic crust and irregular balloons, lopoliths, etc. in the weak ductile crust. In this case, faults controlling emplacement will tend to form circular rather then planar pattern. Further elaboration of the model in 3D will improve our understanding of magmatic channels and emplacement processes.

5. Conclusion

In this study, we examined intrusion processes in numerical experiments incorporating temperature-dependent rheologies of both intrusive molten rocks and host rocks. Experiments were specially designed to investigate the emplacement of mafic and ultramafic magma derived from a sublithospheric source region and rising through the lithosphere in a hot magma channel to reach different levels in the crust. The process did not involve far-field tectonics, whether extensional or compressional.

These model results show that intrusion typically spans a few hundreds kyr spanning three stages: (1) magmatic channel spreading, (2) emplacement and (3) post-intrusive subsidence. The duration of each of these stages strongly depends on the viscosity of ascending magma:

(1) Upward magma transport from sublithospheric depth is driven by the positive buoyancy of the partially-molten rocks with respect to the overriding colder mantle lithosphere. The gravitational balance controls the height of the column of molten rock but not the volume of magmatic rocks below and above the Moho. The molten rocks pool along the crust/mantle boundary only if the lower crust is ductile and very weak, which may be expected at the base of island arcs. It seems natural that otherwise, basic–ultrabasic magma is injected into the crust, most commonly as a funnel-shaped body.
(2) Emplacement within the crust exploits the space opened by the displacement of tectonic crustal blocks bounded by localized zones of intense plastic deformation. Temperature is the important player in controlling crustal viscosities, hence either viscous or elasto-plastic mechanisms of crustal deformation, which defines modes and rates of emplacement. Early normal faults produce early surface subsidence in grabens but rapidly become inverted into thrusts responsible for surface uplift into a large dome structure while the within-crust pluton inflates and rises in the crust.
(3) Late emplacement phases are responsible for flattening of the funnel-shaped body and return magma flow back into the magmatic channel below the Moho. This event is linked to subsidence of the surface.

Models demonstrate, albeit in two-dimensions, that intrusion of high-density magma into low-density crustal rocks is an energetically efficient and mechanically stable process that is less conjectural than one may a priori believe in view of density contrasts. Model results further show that the general shape of the pluton is sensitive to the relative elastic, viscous and plastic parts of the crustal rheology. We conclude that laccolith, lopolith, crescent-shaped and other plutonic shapes have significance concerning the bulk lithospheric rheology. We intend to apply our integrated models to specific cases and extend these results to three-dimensional considerations.

Acknowledgements

This work was supported by ETH Research Grants TH-12/04-1, TH-12/05-3, SNF Research Grant 200021-113672/1 and by the RF President Program "Leading Scientific School of Russia" (grant #НШ-5338.2006.5 to T.V.G.) and the RFBR grant #06-05-64098 (to T.V.G.). Constructive reviews by two anonymous reviewers and editorial handling by G. Schubert are appreciated. P. Tackley is thanked for discussions, comments and improving English.

References

Anderson, D.L., 1994. The sublithospheric mantle as the source of continental flood basalts: the case against the continental lithosphere and plume head reservoirs. Earth Planet. Sci. Lett. 123, 269–280.
Arai, S., Abe, N., Ishimaru, S., 2007. Mantle peridotites from the Western Pacific. Gondwana Res. 11, 180–199.
Bateman, R., 1985. Aureole deformation by flattening around a diapir during in situ balooning: the Cannibal Creek Granite. J. Geol. 93, 293–310.
Bédard, J.H., Sparks, R.S.J., Renner, R., Cheadle, M.J., Hallworth, M.A., 1988. Peridotite sills and metasomatic gabbros in the eastern layered series of the Rhum Complex. J. Geol. Soc. Lond. 145, 207–224.
Bedini, R.-M., Bodinier, J.-L., Dautria, J.M., Morten, L., 1997. Evolution of LILE-enriched small melts fractions in the lithospheric mantle: a case study from the East African Rift. Earth Planet. Sci. Lett. 153, 67–83.
Best, M.G., Christiansen, E.H., 2001. Igneous Petrology. Blackwell Science Inc., Malden, p. 458.
Bittner, D., Schmeling, H., 1995. Numerical modeling of melting processes and induced diapirism in the lower crust. Geophys. J. Int. 123, 59–70.
Bolle, O., Trindade, R.I.F., Bouchez, J.-L., Duchesne, J.-C., 2002. Imaging downward granitic magma transport in the Rogaland Igneous Complex, SW Norway. Terra Nova 14, 87–92.
Borg, L.E., Clynne, M.A., Bullen, T.D., 1997. The variable role of slab-derived fluids in the generation of a suite of primitive calcalkaline lavas from the southernmost Cascades, California. Can. Miner. 35, 425–452.

Brace, W.F., Kohlstedt, D.T., 1980. Limits on lithospheric stress imposed by laboratory experiments. J. Geophys. Res. 85, 6248–6252.

Braun, M.G., Hirth, G., Parmentier, E.M., 2000. The effects of deep damp melting on mantle flow and melt generation beneath mid-ocean ridges. Earth Planet. Sci. Lett. 176, 339–356.

Brenan, J.M., Shaw, H.F., Ryerson, J.F., Phinney, D.L., 1995. Mineral–aqueous fluid partitioning of trace elements at 900 °C and 2.0 GPa: constraints on the trace element chemistry of mantle and deep crustal fluids. Geochim. Cosmochim. Acta 59, 3331–3350.

Brun, J.-P., Pons, J., 1981. Strain patterns of pluton emplacement in a crust undergoing non-coaxial deformation, Sierra Morena, Southern Spain. J. Struct. Geol. 3, 219–229.

Buiter, S.J.H., Babeyko, A.Yu., Ellis, S., Gerya, T.V., Kellner, A., Schreurs, G., Yamada, Y., 2006. The numerical sandbox: comparison of model results for a shortening, an extension experiment. In: Buiter, S.J.H., Schreurs, G. (Eds.), Analogue and Numerical Modelling of Crustal-Scale Processes, vol. 253. Geological Society, Special Publications, London, pp. 29–64.

Burg, J.-P., Gerya, T.V., 2005. Viscous heating and thermal doming in orogenic metamorphism: numerical modeling and geological implications. J. Metamorphic Geol. 23, 75–95.

Clauser, C., Huenges, E., 1995. Thermal conductivity of rocks, minerals. In: Ahrens, T.J. (Ed.), Rock Physics and Phase Relations. American Geophysical Union, Washington, DC, pp. 105–126.

Clemens, J.D., Mawer, C.K., 1992. Granitic magma transport by fracture propagation. Tectonophysics 204, 339–360.

Coffin, M.F., Eldholm, O., 1994. Large igneous provinces: crustal structure, dimensions, and external consequences. Rev. Geophys. 32, 1–36.

Connolly, J.A.D., Podladchikov, Y.Y., 1998. Compaction-driven fluid flow in viscoelastic rock. Geodinamica Acta 11, 55–84.

Cruden, A., 1990. Flow and fabric development during the diapiric rise of magma. J. Geol. 98, 681–698.

Cruden, A.R., McCaffrey, K.J.W., 2001. Growth of plutons by floor subsidence: implications for rates of emplacement, intrusion spacing and melt-extraction mechanisms. Phys. Chem. Earth Part A: Solid Earth Geodesy 26, 303–315.

Dungan, M.A., Wulff, A., Thompson, R., 2001. Eruptive stratigraphy of the Tatara-San Pedro Complex, 36°S, southern volcanic zone. Chilean Andes: reconstruction method and implications for magma evolution at long-lived arc volcanic centers. J. Petrol. 42, 555–626.

Elianov, A.A., Andreev, G.V., 1991. Magmatism and metallogeny of platform areas of multistage activation. Nauka, Novosibirsk, 168 (in Russian).

Ellenberger, F., 1994. Histoire de la Géologie. La grande éclosion et ses prémices. Petite Collection D'histoire Des Sciences. 2. Technique et Documentation, Lavoisier, Paris, p. 381.

Ernst, R.E., Buchan, K.L., Campbell, I.H., 2005. Frontiers in large igneous province research. Lithos 7, 271–297.

Furlong, K.P., Meyers, J.D., 1985. Thermal–mechanical modeling of the role of thermal stresses in magma contamination. J. Volcanol. Geotherm. Res. 24, 179–191.

Gerya, T.V., Yuen, D.A., 2003a. Characteristics-based marker-in-cell method with conservative finite-differences schemes for modeling geological flows with strongly variable transport properties. Phys. Earth Planet. Interiors 140, 295–320.

Gerya, T.V., Yuen, D.A., 2003b. Rayleigh-Taylor instabilities from hydration and melting propel "cold plumes" at subduction zones. Earth Planet. Sci. Lett. 212, 47–62.

Gerya, T.V., Perchuk, L.L., Van Reenen, D.D., Smit, C.A., 2000. Two-dimensional numerical modeling of pressure–temperature–time paths for the exhumation of some granulite facies terrains in the Precambrian. J. Geodynamics 29, 17–35.

Gerya, T.V., Uken, R., Reinhardt, J., Watkeys, M.K., Maresch, W.V., Clarke, B.M., 2003. Cold fingers in a hot magma: numerical modeling of diapirs in the Bushveld Complex, South Africa. Geology 31, 753–756.

Gerya, T.V., Yuen, D.A., Sevre, E.O.D., 2004a. Dynamical causes for incipient magma chambers above slabs. Geology 32, 89–92.

Gerya, T.V., Uken, R., Reinhardt, J., Watkeys, M.K., Maresch, W.V., Clarke, B.M., 2004. "Cold" domes and diapirs triggered by the Bushveld magmatic event: insight from 2-D numerical modeling. In: Whitney, D., Teyssier, C., Siddoway, C.S. (Eds.), Gneiss Domes in Orogeny. GSA Special Paper 380, pp. 117–127.

Gerya, T.V., Connolly, J.A.D., Yuen, D.A., Gorczyk, W., Capel, A.M., 2006. Sesmic implications of mantle wedge plumes. Phys. Earth Planet. Interiors 156, 59–74.

Glazner, A.F., Bartley, J.M., Coleman, D.S., Gray, W., Taylor, R.Z., 2004. Are plutons assembled over millions of years by amalgamation from small magma chambers? Geol. Soc. Am. Today 14, 4–11.

Gorczyk, W., Gerya, T.V., Connolly, J.A.D., Yuen, D.A., Rudolph, M., 2006. Large-scale rigid-body rotation in the mantle wedge and its implications for seismic tomography. Geochem. Geophys. Geosyst. 7 (art. no. Q05018).

Harry, D.L., Green, N.L., 1999. Slab dehydration and basalt petrogenesis in subduction systems involving very young oceanic lithosphere. Chem. Geol. 160, 309–333.

Head III, J.W., Coffin, M.L., 1997. Large igneous provinces: a planetary perspective. In: Mahoney, J.J., Coffin, M.F. (Eds.), Large Igneous Provinces—Continental, Oceanic and Planetary Flood Volcanism. Am. Geophys. Union Geophys. Monogr. 100, pp. 411–438.

Hess, P.C., 1989. Origin of Igneous Rocks. Harward University Press, London, p. 490.

Hogan, J.P., Gilbert, M.C., 1997. The intrusive style of A-type sheet granites from the Southern Oklahoma Aulacogen. In: Ojakangas, R.W., Dickas, A.B., Green, J.C. (Eds.), Middle Proterozoic to Cambrian rifting, Mid-North America. Geol. Soc. America, Special Paper, pp. 299–311.

Hutton, D.H.W., 1988. Granite emplacement mechanisms and tectonic controls: inferences from deformation studies. Trans. R. Soc. Edinburgh Earth Sci. 79, 245–255.

Irvine, T.N., 1967. The Duke Island ultramafic complex, southeastern Alaska. In: Wyllie, P.J. (Ed.), Ultramafic and Related Rocks. John Wiley & Sons, New York, pp. 84–97.

Iwamori, H., 1991. Zonal structure of Cenozoic basalts related to mantle upwelling in southwest Japan. J. Geophys. Res. 96, 6157–6170.

Kogarko, L.N., 1987. Alkaline rocks of the eastern part of the Baltic Shield (Kola Peninsula). In: Fitton, J.G., Upton, B.G.J. (Eds.), Alkaline Igneous Rocks, vol. 30. Geological Society Special Publication, pp. 531–544.

Lin, S.C., Kuo, B.Y., Chiao, L.Y., van Keken, P.E., 2005. Thermal plume models and melt generation in East Africa: a dynamic modeling approach. Earth Planet. Sci. Lett. 237, 175–192.

Maclennan, J., Lovell, B., 2002. Control of regional sea level by surface uplift and subsidence caused by magmatic underplating of Earth's crust. Geology 30, 675–678.

Marsh, B.D., 1982. On the mechanics of igneous diapirism, stoping, and zone melting. Am. J. Sci. 282, 808–855.

McCulloch, M.T., Gamble, J.A., 1991. Geochemical and geodynamical constraints on subduction zone magmatism. Earth Planet. Sci. Lett. 102, 358–374.

Mjelde, R., Kasahara, J., Shimamura, H., Kamimura, A., Kanazawa, T., Kodaira, S., Raum, T., Shiobara, H., 2002. Lower crustal seismicity velocity-anomalies: magmatic underplating or serpentinized peridotite? Evidence from the Vøring Margin, NE Atlantic. Mar. Geophys. Res. 23, 169–183.

Montesi, L.G.J., 2001. Concentric dikes on the flanks of Pavonis Mons: implications for the evolution of martian shield volcanoes and mantle plumes. In: Ernst, R.E., Buchan, K.L. (Eds.), Mantle Plumes: Their Identification Through Time. Special Paper, Geol. Soc. Am. 352, 165–181.

Moresi, L., Dufour, F., Mühlhaus, H.-B., 2003. A Lagrangian integration point finite element method for large deformation modeling of viscoelastic geomaterials. J. Comput. Phys. 184, 476–497.

Muentener, O., Hermann, J., Trommsdorff, V., 2000. Cooling history and exhumation of lower-crustal granulite and upper mantle (Malenco, eastern Central Alps). J. Petrol. 41, 175–200.

Parsons, I., Becker, S.M., 1987. Layering, compaction and post-magmatic processes in the Klokken intrusion. In: Parsons, I. (Ed.), Origins of Igneous Intrusions. NATO ASI Series C: Mathematical and Physical Sciences. D. Reidel Publishing Company, Dordrecht, pp. 29–92.

Paterson, S.R., Fowler, K., 1993. Re-examining pluton emplacement processes. J. Struct. Geol. 15, 191–206.

Petford, N., 1996. Dykes or diapirs? Trans. R. Soc. Edinburgh Earth Sci. 87, 105–114.

Petford, N., Cruden, A.R., McCaffrey, K.J., Vigneresse, J.-L., 2000. Granite magma formation, transport and emplacement in the Earth's crust. Nature 408, 669–673.

Petrini, K., Podladchikov, Y., 2000. Lithospheric pressure–depth relationship in compressive regions of thickened crust. J. Metamorphic Geol. 18, 67–77.

Pinkerton, H., Stevenson, R.J., 1992. Methods of determining the rheological properties of magmas at subliquidus temperatures. J. Volcanol. Geotherm. Res. 53, 47–66.

Pitcher, W.S., 1979. The nature, ascent and emplacement of granitic magma. J. Geol. Soc. Lond. 136, 627–662.

Pons, J., Oudin, C., Valero, J., 1992. Kinematics of large syn-orogenic intrusions: example of the Lower Proterozoic Saraya batholith (Eastern Senegal). Geologische Rundschau 81, 473–486.

Rabinowicz, M., Ceuleneer, G., 2005. The effect of sloped isotherms on melt migration in the shallow mantle; a physical and numerical model based on observations in the Oman ophiolite. Earth Planet. Sci. Lett. 229, 231–246.

Ramberg, H., 1981. The role of gravity in orogenic belts. In: McClay, K.R., Price, N.J. (Eds.), Thrust and Nappe Tectonics. Geological Society Special Publication, London, pp. 125–140.

Ranalli, G., 1995. Rheology of the Earth. Chapman & Hall, London, p. 413.

Ricard, Y., Bercovici, D., Schubert, G., 2001. A two-phase model for compaction and damage. 2. Applications to compaction, deformation, and the role of interfacial surface tension. J. Geophys. Res. 106, 8907–8924.

Rudnick, R., 1995. Making continental crust. Nature 378, 571–578.

Rudnick, R., Gao, S., 2004. The composition of the continental crust. In: Rudnick, R. (Ed.), Treatise on Geochemistry: The Crust. Elsevier, Amsterdam, pp. 1–64.

Scambelluri, M., Philippot, P., 2001. Deep fluids in subduction zones. Lithos 55, 213–227.

Schmidt, M.W., Poli, S., 1998. Experimentally based water budgets for dehydrating slabs and consequences for arc magma generation. Earth Planet. Sci. Lett. 163, 361–379.

Schwerdtner, W.M., Stott, G.M., Sutcliffe, R.H., 1983. Strain patterns of crescentic granitoid plutons in the Archean greenstone terrain of Ontario. J. Struct. Geol. 5, 419–430.

Scott, D.R., Stevenson, D.J., 1986. Magma ascent by porous flow. J. Geophys. Res. 91, 9283–9296.

Sleep, N.H., 2006. Mantle plumes from top to bottom. Earth Sci. Rev. 77, 231–271.

Sparks, D.W., Parmentier, E.M., 1991. Melt extraction from the mantle beneath spreading centers. Earth Planet. Sci. Lett. 105, 368–377.

Sparks, R.S.J., Huppert, H.E., Kerr, R.C., McKenzie, D.P., Tait, S.R., 1985. Postcumulus processes in layered intrusions. Geol. Mag. 122, 555–568.

Spera, F.J., 1980. Aspects of magma transport. In: Hargraves, R.B. (Ed.), Physics of Magmatic Processes. Princeton University Press, Princeton, pp. 263–323.

Spiegelman, M., Kelemen, P.B., 2003. Extreme chemical variability as a consequence of channelized melt transport. Geochem. Geophys. Geosyst. 4, Art. No. 1055.

Stel, H., 1991. Linear dilatation structures and syn-magmatic folding in granitoids. J. Struct. Geol. 13, 625–634.

Taylor Jr., H.P., 1967. The zoned ultramafic complexes of southeastern Alaska. In: Wyllie, P.J. (Ed.), Ultramafic and Related Rocks. John Wiley and Sons, New York, pp. 97–121.

Turcotte, D.L., Schubert, G., 2002. Geodynamics. Cambridge University Press, Cambridge, p. 456.

Turner, S., Evans, P., Hawkesworth, C., 2001. Ultrafast source-to-surface movement of melt at island arcs from ^{226}Ra–^{230}Th systematics. Science 292, 1363–1366.

Turner, S.P., George, R.M.M., Evans, P.J., Hawkesworth, C.J., Zellmer, G.F., 2000. Time-scales of magma formation, ascent and storage beneath subduction-zone volcanoes. Philos. Trans. R. Soc. Lond. A358, 1443–1464.

Vasilyev, O.V., Podladchikov, Y.Y., Yuen, D.A., 1998. Modeling of compaction driven flow in poro-viscoelastic medium using adaptive wavelet collocation method. Geophys. Res. Lett. 25, 3239–3242.

Vigneresse, J.-L., 1995. Control of granite emplacement by regional deformation. Tectonophys 249, 173–186.

Vigneresse, J.-L., Clemens, J.D., 2000. Granitic magma ascent and emplacement: neither diapirism nor neutral buoyancy. In: Vendeville, B., Mart, Y., Vigneresse, J.-L. (Eds.), Salt, Shale and Igneous Diapirs In and Around Europe. Geological Society Special Publication, London, pp. 1–19.

Wright, T.L., Klein, F.W., 2006. Deep magma transport at Kilauea volcano. Hawaii. Lithos 87, 50–79.

Wyllie, P.J., 1967. Ultramafic and Related Rocks. John Wiley & Sons Inc., New York, p. 464.

Xu, Y.-G., Menzies, M.A., Bodinier, J.-L., Bedini, R.M., Vroon, P., Mercier, J.-C.C., 1998. Melt percolation and reaction atop a plume: evidence from the poikiloblastic peridotite xenoliths from Borée (Massif Central France). Contrib. Miner. Petrol. 132, 65–84.